Role of molecular oxygen in the dissolution of siderite and rhodochrosite

OWEN W. DUCKWORTH and SCOT T. MARTIN*

Division of Engineering and Applied Sciences, Pierce Hall, 29 Oxford Street, Harvard University, Cambridge, MA 02138, USA

Abstract—The dissolution of siderite ($FeCO_3$) and rhodochrosite ($MnCO_3$) under oxic and anoxic conditions is investigated at 298 K. The anoxic dissolution rate of siderite is $10^{-8.65}$ mol m^{-2} s^{-1} for $5.5 < pH < 12$ and increases as $[H^+]^{0.75}$ for $pH < 5.5$. The pH dependence is consistent with parallel proton-promoted and water hydrolysis dissolution pathways. Atomic force microscopy (AFM) reveals a change in pit morphology from rhombohedral pits for $pH > 4$ to pits elongated at one vertex for $pH < 4$. Under oxic conditions the dissolution rate decreases to below the detection limit of 10^{-10} mol m^{-2} s^{-1} for $6.0 < pH < 10.3$, and hillock precipitation preferential to steps is observed in concurrent AFM micrographs. X-ray photoelectron spectroscopy (XPS) and thermodynamic analysis identify the precipitate as ferrihydrite. At $pH > 10.3$, the oxic dissolution rate is as high as $10^{-7.5}$ mol m^{-2} s^{-1}, which is greater than under the corresponding anoxic conditions. A fast electron transfer reaction between solution O_2 or $[Fe^{3+}(OH)_4]^-$ species and surficial $>Fe^{II}$ hydroxyl groups is hypothesized to explain the dissolution kinetics. AFM micrographs do not show precipitation under these conditions. Anoxic dissolution of rhodochrosite is physically observed as rhombohedral pit expansion for $3.7 < pH < 10.3$ and is chemically explained by parallel proton- and water-promoted pathways. The dissolution rate law is $10^{-4.93}[H^+] + 10^{-8.45}$ mol m^{-2} s^{-1}. For $5.8 < pH < 7.7$ under oxic conditions, the AFM micrographs show a tabular precipitate growing by preferential expansion along the a-axis, though the macroscopic dissolution rate is apparently unaffected. For $pH > 7.7$ under oxic conditions, the dissolution rate decreases from $10^{-8.45}$ to $10^{-9.0}$ mol m^{-2} s^{-1}. Flattened hillock precipitates grow across the entire surface without apparent morphological influence by the underlying rhodochrosite surface. XPS spectra and thermodynamic calculations implicate the precipitate as bixbyite for $5.8 < pH < 7.7$ and MnOOH (possibly feitnkechtite) for $pH > 7.7$. *Copyright © 2004 Elsevier Ltd*

1. INTRODUCTION

Rhodochrosite ($MnCO_3$) and siderite ($FeCO_3$) are important reduced phase minerals that occur in terrestrial and marine deposits and sedimentary rocks (Curtis et al., 1975; Postma, 1977, 1981, 1982; Barhrig, 1985; Dresel, 1989; Bruno et al., 1992; Klein and Hurlbut, 1993; McBride, 1994; Calvert and Pedersen, 1996; Huckriede and Meischner, 1996; Sternbeck, 1997; Kelts, 1998; McMillan and Schwertmann, 1998). Their solubility limits aqueous Fe and Mn concentrations under anoxic conditions in many diverse environments (Morgan, 1967; Li et al., 1969; Cavert and Price, 1972; Middelburg et al., 1987; Wersin et al., 1989; Amirbahman et al., 1998; Jensen et al., 2002). Under oxic and mildly alkaline conditions, $FeCO_3$ and $MnCO_3$ solubility is complicated by oxidation of the released $Fe^{2+}(aq)$ and $Mn^{2+}(aq)$ and subsequent precipitation of Fe^{III} and $Mn^{III/IV}$ (hydr)oxide minerals, which are orders of magnitude less soluble than the parent carbonate material (Dresel, 1989; Huckriede and Meischner, 1996; McMillan and Schwertmann, 1998; La Force et al., 2002). The interconversions among mineral phases are episodic and seasonal, varying with temporal changes in local pE and pH (Huckriede and Meischner, 1996; La Force et al., 2002). Solubility may be further complicated by morphology: hysteresis in dissolution behavior occurs when (hydr)oxide minerals precipitate as insoluble coatings on the surfaces of carbonate grains and thus kinetically inhibit dissolution even in cases where carbonate dissolution is highly favored thermodynamically (Dresel, 1989). Dissolution and precipitation are significant in the biogeochemical cycling not only of Fe and Mn but also of other metals (e.g., U, Co, Pb, Ni, Cu, and Zn) that coprecipitate with Fe and Mn (hydr)oxides (Jenne, 1968; Hem, 1978; Hem et al., 1989; Duff et al., 2002).

In the natural environment, cycling of Fe and Mn occurs at oxic/anoxic interfaces where precipitation and dissolution occur simultaneously. Accurate understanding of biogeochemical cycling thus requires a quantitative description of the effects of O_2. Molecular oxygen (O_2) plays a critical role in determining the bioavailability of Fe and Mn due to the great solubility difference between $Fe^{III}/Mn^{III/IV}$ (hydr)oxides and Fe^{II}/Mn^{II} carbonates. If equilibrium conditions prevail, understanding the effects of O_2 is straightforward: a thermodynamic analysis would provide both the mix of solids present and the aqueous (i.e., bioavailable) concentrations of Fe and Mn species. However, the equilibrium treatment fails for two important reasons. First, surface-controlled dissolution and precipitation rates may be slow. Second, morphologic features such as precipitation of an oxide supralayer may armor the carbonate surface and significantly reduce dissolution rates. Understanding the effects of O_2 on the dynamics of dissolution requires a kinetic chemical transport description.

In this study, we quantify the dissolution rates of the $(10\bar{1}4)$ face of $FeCO_3$ and $MnCO_3$ under oxic and anoxic conditions for $1.5 < pH < 12$ at 298 K. Concurrently, atomic force microscopy is utilized to observe changes in the morphology of pits and the appearance of secondary mineral precipitates. X-ray photoelectron spectroscopy is employed to identify the chemical composition of these (hydr)oxide precipitates. We

* Author to whom correspondence should be addressed (smartin@deas.harvard.edu).

find that thermodynamic analyses rationalize and bring cohesion to a variety of complex and interrelated data sets (e.g., the effects of P_{O2} and pH on a time series of AFM images, dissolution rates, and XPS spectra).

2. EXPERIMENTAL METHODOLOGY

2.1. Materials

Crystals of rhodochrosite (sample 96030, Colorado) and siderite (sample 134827, Ivigtut, Greenland) are obtained from the Harvard University Mineralogical Museum. Mineral identity and the absence of other phases (nominal detection limit = 2%) are confirmed with X-ray diffraction (Phillips X-ray diffractometer). Proton-induced X-ray emission spectroscopy (PIXE, Cambridge accelerator for materials science (CAMS), Harvard University) is utilized to determine the concentrations of cation impurities in the surface regions of the samples. PIXE analysis of siderite shows an Fe purity of 95.35%, with 4.47% Mn and trace amounts (<0.04%) of Zn, Ca, and Sr. Other cations, including Cd, Ni, and Pb, are below the minimum detection limit, which ranges from 0.001–0.04% cation mole percent. The composition of rhodochrosite samples (99.59% Mn purity) is reported previously (Duckworth and Martin, 2003).

The $MnCO_3$ and $FeCO_3$ crystals are cleaved with a razor blade along the $\{10\bar{1}4\}$ plane (perfect cleavage). We employ the Miller indices conventions of O'Keeffe and Hyde (1996). The cleaved samples are pressed into warmed dental modeling wax (Cavex, Holland) for attachment to a steel puck. The wax covers the edges of the sample so that only the imaged surface dissolves. Control experiments conducted with calcite yield step velocities, pit morphologies, and dissolution rates that agree well with prior studies (Shiraki et al., 2000). A new surface is prepared for each experiment. The geometric surface area (A) is calculated by employing Photoshop (Adobe Systems, San Jose, CA) to analyze digital photographs.

Aqueous solutions at several pH values are prepared on the day of each experiment by purging deionized water with argon or oxygen (0.5 L min^{-1}) for 2 h. This purged water is titrated with solutions made with HCl (EM OmniTrace grade) or NaOH (Aldrich, 99.998%) to set pH. Solution ionic strength resulting from Na$^+$ and Cl$^-$ ions added to set pH is less than 35 mM. Ionic strength ranging from near zero to 10 mM negligibly affects carbonate dissolution rates (Pokrovsky and Schott, 2001; Friis et al., 2003). Prepared solutions are immediately drawn into 60 mL plastic syringes and capped until use. The upper limit of P_{O2} of the argon-purged solutions (<0.01 atm) is determined with a dissolved oxygen meter (Strathkelvin Instruments Model 781, Glasgow, Scotland).

2.2. Simultaneous AFM/Flow-Through Reactor Experiments

The apparatus utilized in the simultaneous AFM/flow-through reactor experiments is previously described (Duckworth and Martin, 2003). A crystal affixed to a steel puck is placed on the end of the AFM piezoelectric scanner, and a drop of deoxygenated solution is placed on the sample. This step is necessary to avoid bubbles that prevent imaging in the fluid cell. The fluid cell is immediately placed over the sample to minimize exposure to atmospheric oxygen, which causes detectable surface oxidation within 30 min at neutral pH. A dissolution liquor is pumped through the fluid cell at 0.01–1.5 mL min^{-1}. At a chosen time, the syringe is switched so as to change the pH and pE conditions in the cell.

Graphite furnace atomic absorption spectroscopy (GF-AAS, AAnalyst 300 atomic absorption spectrometer equipped with an HGA 850 graphite furnace, Perkin-Elmer) is employed to determine aqueous metal concentration in the effluent from the liquid cell. For our experimental conditions, the GF-AAS limit of detection is Mn$_T$ = 2 nM and Fe$_T$ = 4 nM, where Mn$_T$ and Fe$_T$ are the total aqueous metal concentration, i.e., the sum of the concentrations of all aqueous species of Mn^{2+} and Fe^{2+}/Fe^{3+}, respectively. Aqueous Mn^{3+} and Mn^{4+} are not considered in our system because are they are insoluble under our experimental conditions and thus contribute negligibly to Mn$_T$.

An atomic force microscope is employed to image the surface in contact mode (Nanoscope IIIa Multimode SPM, Digital Instruments) at 1 to 4 Hz with oxide-sharpened silicon nitride probes (nominal radius of curvature of 5–40 nm and force constant of 0.12 N m^{-1}) while solution flows through the AFM cell. Images collected in the same scan direction (i.e., exclusively upscans or downscans) are employed for analysis. Possible artifacts induced by imaging, such as scan fields, are examined by periodically scanning normal to the original direction and by comparing images where the tip has rastered for several hours (e.g., during an experiment to collect a time series of images) to an image where the tip has scanned only once. Duckworth and Martin (2003) and Shiraki et al. (2000) demonstrate that microscopic observations quantitatively agree with macroscopic dissolution rates, suggesting that the microscopic area imaged is representative of the overall dissolution processes occurring on the surface.

2.3. Dissolution Rates

Dissolution rates are calculated from the metal ion flux through the fluid cell, as follows (Shiraki et al., 2000; Duckworth and Martin, 2003):

$$R = \frac{\Delta M_T q}{A} \qquad (1)$$

where R (mol m^{-2} s^{-1}) is the dissolution rate, ΔM_T (M) is the difference in Fe$_T$ or Mn$_T$ between the influent and the effluent, q is the flow rate (L s^{-1}), and A is the geometric surface area (m^2) of the sample. In our experiments, the inlet concentration is below the limit of detection (i.e., Mn$_T$ < 2 nM and Fe$_T$ < 4 nM) while the effluent concentration varies from 2 to 4000 nM. In control experiments, we verify that the dissolution rate is independent of q.

2.4. X-Ray Photoelectron Spectroscopy (XPS)

$MnCO_3$ and $FeCO_3$ are exposed to solutions of variable pH, dried, and analyzed ex situ by XPS. Spectra are collected for these samples as well as several reference minerals, including pyrolusite (Atikokan, Ontario), manganite (Atikokan, Ontario), hematite (sample 92687, San Jose, Costa Rica), lepidocrocite (J.B. Pearce Collection Sample, Germany), and unreacted $MnCO_3$ and $FeCO_3$. A Surface Science Laboratories SSX-100 X-ray photoelectron spectrometer, equipped with a monochromatized Al Kα X-ray source and characterized by a base pressure of 10^{-9} Torr in the analytical chamber, is employed. Scans of the Mn, Fe, O, and C energies are recorded using a fixed pass energy of 50 eV and 600 μm spot size. The C 1s adventitious carbon peak (284.6 eV) is used to correct binding energies, which is necessary due to surface charging (Wagner et al., 1979). Previous workers also utilize the adventitious carbon peak as a reference to examine the chemical bonding of oxygen in mineral surfaces (McIntyre and Zetruk, 1975; Harvey and Linton, 1981; Sosulnikov and Teterin, 1992; Ding et al., 2000).

2.5. Thermodynamic Calculations

MINEQL+ (Environmental Research Software, Hallowell, ME) is employed to calculate the equilibrium aqueous speciation and the saturation ratios of solids under our experimental conditions. The saturation ratio, S, is defined as follows: $S = (Q/K_{sp})$ where Q is the reaction quotient and K_{sp} is the solubility product. Formation constants of aqueous species and the solubility products of solid phases are provided in a critically reviewed database within MINEQL+ (Schecher, 2001). We also incorporate the K_{sp} value of feitknechtite (Hem et al., 1982) into the MINEQL+ database. Solubility calculations for Fe^{III}, Mn^{III}, and Mn^{IV} (hydr)oxides assume P_{O2} = 1 atm, while those for $FeCO_3$ and $MnCO_3$ assume P_{O2} = 0 atm.

3. RESULTS

Figure 1A shows typical time course profiles of pH and Fe$_T$ during an anoxic experiment with $FeCO_3$. pH rapidly attains a steady-state value, both at the start of the experiment and after a change in influent. After an initial transient at the beginning of the experiment, Fe$_T$ also reaches a steady-state concentration
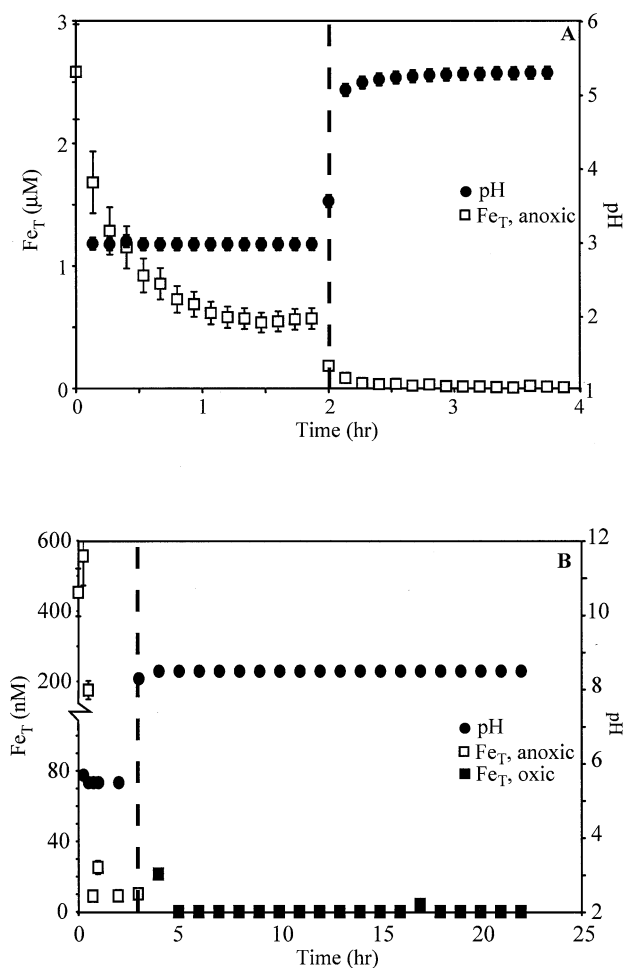
Fig. 1. Time series profiles of pH and Fe_T in $FeCO_3$ dissolution experiments. (A) A change in inlet solution pH from 3 to 5 under anoxic conditions occurs at the dashed vertical line. (B) A change in inlet solution pH from 5.5 to 8.5 and P_{O2} from 0 to 1 atm occurs at the dashed vertical line. From the Fe_T data, the dissolution rate (mol m^{-2} s^{-1}) is calculated by Eqn. 1.
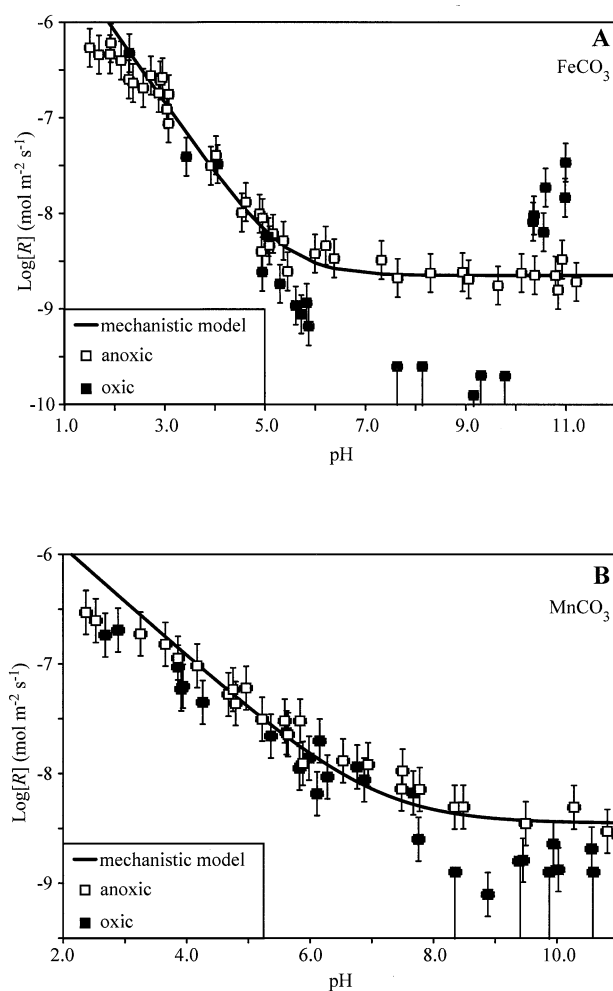

Fig. 2. Dissolution rate of the $(10\bar{1}4)$ faces of (A) $FeCO_3$ and (B) $MnCO_3$ as a function of pH under oxic and anoxic conditions. A solid line shows a fit by a mechanistic model to the anoxic data (see text). Uncertainty bars that extend to the x-axis indicate upper limits for dissolution rates (i.e., Fe_T or Mn_T is below the limit of detection of our analytical method).

for each pH value. The initial transient possibly arises from the dissolution of high-energy sites created when cleaving the mineral or from the initial rapid formation of deep pits at dislocations. Steady-state dissolution rates for a selected pH value are calculated from the average Fe_T at steady-state, as by Eqn. 1. The dissolution rates are calculated in this manner under anoxic (R_{an}) and oxygen-saturated conditions (R_{ox}).

Figure 1B shows typical time course profiles of pH and Fe_T during an oxic experiment with $FeCO_3$. Anoxic solution is initially pumped into the fluid cell to prepare the surface and eliminate initial transients, which typically occur during the first hour of reaction (cf. Fig. 1A). The inlet solution is then switched to an oxygen-saturated solution at the desired pH. None of the time course profiles of Fe_T or Mn_T, including when surface precipitates are observed in the AFM micrographs, shows decay during the timescale of our experiments.

Dissolution rates R_{an} and R_{ox} are summarized in Figure 2 for $FeCO_3$ and $MnCO_3$. For $FeCO_3$ (Fig. 2A), $R_{an} = 10^{-8.65}$ mol m^{-2} s^{-1} for $5.5 < pH < 12$ and increases steadily for

pH < 5.5. For pH < 5, the presence of oxygen does not affect the dissolution rate (i.e., $R_{an=Rox}$). However, for $6 < pH < 10.3$, R_{ox} is below the limit of detection. For pH > 10.3, R_{ox} is as high as $10^{-7.5}$ mol m^{-2} s^{-1}, which is greater than under the corresponding anoxic conditions. For $MnCO_3$ (Fig. 2B), $R_{an} = 10^{-8.45}$ mol m^{-2} s^{-1} for $7 < pH < 11$ and increases steadily for pH < 7. For pH < 7.7, the presence of oxygen does not affect the dissolution rate (i.e., $R_{an=Rox}$). For pH > 7.7 R_{ox} is reduced 80% with respect to R_{an}.

Figure 3 shows time series of pits typical of anoxic dissolution at all pH values and of oxic dissolution at acidic pH. The image series for $FeCO_3$ (Fig. 3, left) begins shortly after the pH is adjusted to 1.9 from a neutral solution. Deep pits (100–1500 nm depth) with a rhombohedral morphology expand on the surface terrace regions. The internal angles (78° and 102°) of 3A indicate that the pits are bound by vicinal $[\bar{4}41]$ and $[48\bar{1}]$ crystallographic vectors, as is known for the isostructural carbonate family at pH > 4, including rhodochrosite (Duckworth
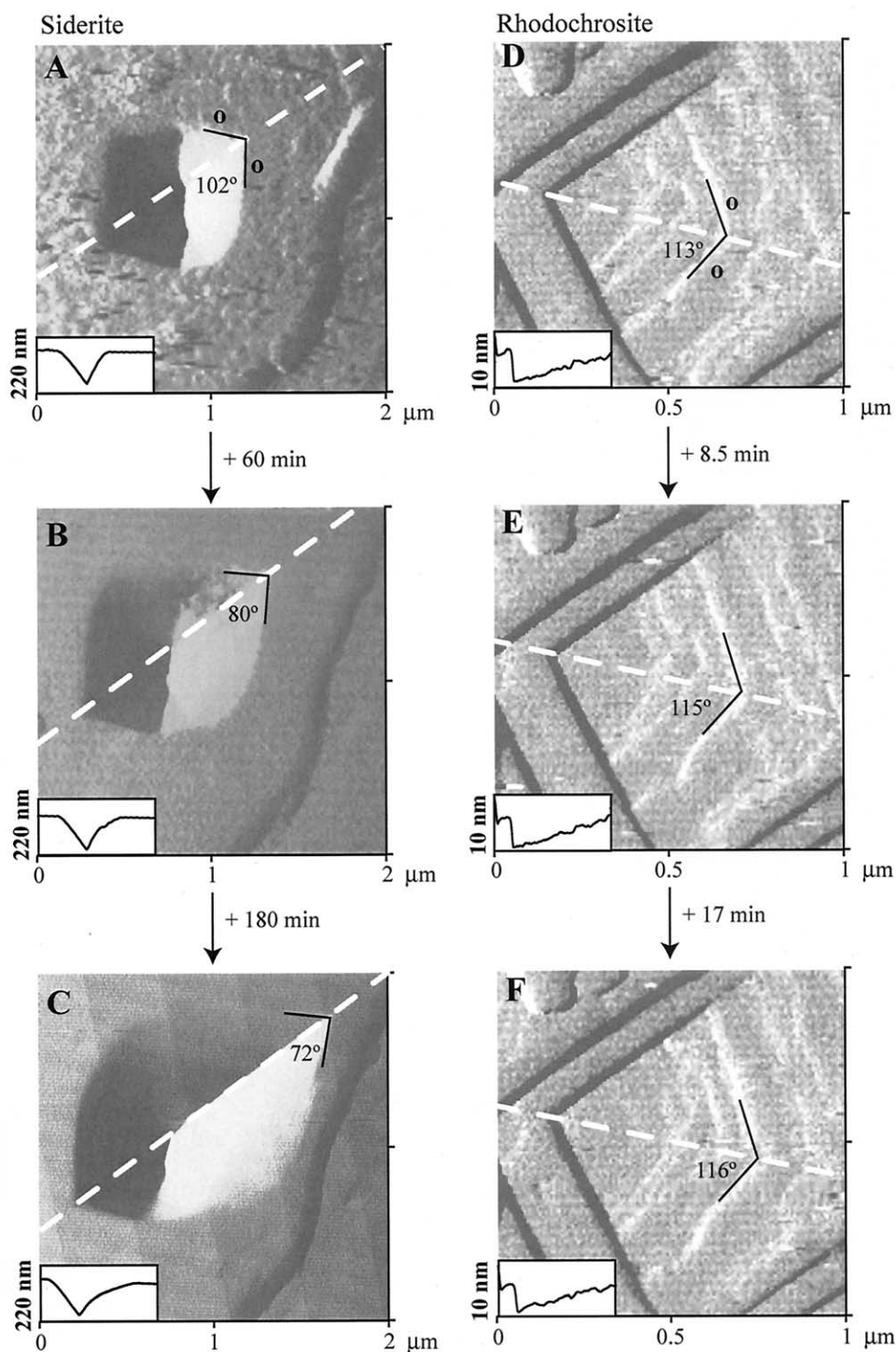
Fig. 3. Time series of AFM deflection mode micrographs of pits typical of anoxic and low pH oxic conditions. (A-C) A deep pit on the ($10\bar{1}4$) face of $FeCO_3$ at pH = 1.9 in the presence of O_2 (1 atm). (D-F) A shallow flat-bottomed pit on the ($10\bar{1}4$) face of $MnCO_3$ at pH = 3.6 in the absence of O_2. Inset: Height mode cross sections shown for dashed white lines.

and Martin, 2003), magnesite (Jordan et al., 2001), and calcite (Hillner et al., 1992; MacInnis and Brantley, 1992; Liang et al., 1996b). Pit expansion by step retreat is anisotropic: for most aqueous chemical conditions, steps that are obtuse at the atomic level (i.e., underhanging) retreat more rapidly than those that

are acute (i.e., overhanging). In our images, we then identify the obtuse steps by a fast retreat rate, as compared to the acute steps, at circumneutral pH (Liang and Baer, 1997; Shiraki et al., 2000).

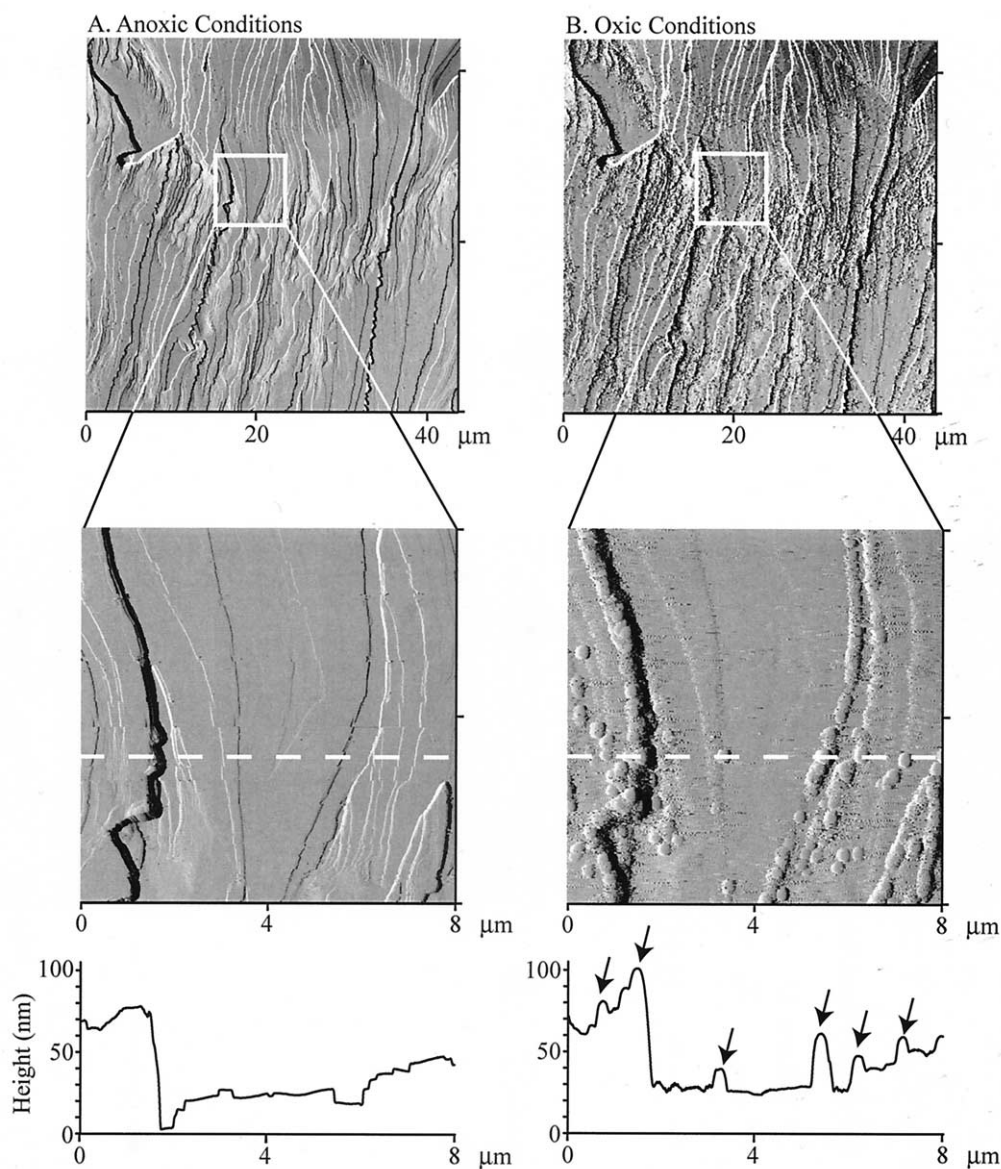In Figure 3A, a contaminant layer is apparent on the terrace

Fig. 4. AFM deflection mode micrographs and height mode cross sections showing the effect of O_2 at pH = 9.2 on the $(10\bar{1}4)$ face of $FeCO_3$.(A) Anoxic solution at pH = 4.6. (B) Micrographs recorded 21 h after exposure to O_2 at pH = 9.2. Higher resolution micrographs collected for regions indicated by white boxes in the top images are shown in the middle images. Small hillock precipitates (10–20 nm height by 100–200 nm diameter) form preferentially at step sites, as indicated by arrows in cross-section analysis (bottom).

regions surrounding the pit. This type of contaminant, commonly observed on the surface of $FeCO_3$, is weakly associated with the surface and is removed easily by scanning the AFM tip, both in air and under solution. The contaminant also disappears rapidly at high pH. We believe this contaminant is a loosely afixed oxidized layer formed after cleavage of the mineral and exposure to air or solution containing trace of atmospheric oxygen that diffuses into the initial drop of solution during the mounting of the fluid cell.

Pit morphology often distorts at low pH. As shown in Figures 3B,C for $FeCO_3$, at pH = 1.9 the pits grow with an extension at the obtuse steps and a corresponding reduction in the angle between obtuse steps. At steady-state this angle changes with pH from 102° at pH > 4 to 72° at pH = 1.9. An image for pH > 4 is not shown due to its similarity to Figure 3A. The morphology under oxic conditions for pH < 4 is identical to that observed under anoxic conditions. A change in step orientation at low pH is known for magnesite and explained by a change in atomic scale step-kink dynamics (Jordan et al., 2001). In contrast to the behavior observed for siderite at low pH, rhodochrosite pit morphology alters by a slight widening of the angle between obtuse steps from 102° at circumneutral pH (fig. 4 of Duckworth and Martin, 2003) to 116° at low pH, while the angle between acute steps does not change (Figs. 3D–F, pH = 3.6). Slight rounding of pit corners and increased step raggedness also occurs.

Figure 4 shows how exposure to O_2(aq) in circumneutral to mildly alkaline pH affects the $(10\bar{1}4)$ face of $FeCO_3$ at a scale (40 μm × 40 μm) larger than that shown for pits in Figure 3. Figure 4A shows the surface in aqueous solution at pH = 4.6 before oxygen exposure. The inlet solution is changed to an oxygen-saturated solution at pH = 9.2, and the surface is then imaged every few hours for the next 21 h. The final image in the time series (Fig. 4B) shows that hillock precipitates form (100–200 nm diameter and 10–20 nm height). The hillock contact angle, as measured from cross sections, is 10 ± 3° (Rieutord and Salmeron, 1998). These hillocks form predominantly at the top of steps. Figure 2A shows a large decrease in macroscopic dissolution rates concurrent with the AFM observations of the hillock precipitation (6 < pH < 10.3).

Figure 5 shows how exposure to O_2(aq) in circumneutral to mildly alkaline pH affects the $(10\bar{1}4)$ face of $MnCO_3$ at the mesoscale (40 μm × 40 μm). A fresh $MnCO_3$ surface imaged in anoxic solution at pH = 3.7 is shown in Figure 5A, and a step and terrace morphology typical of the $(10\bar{1}4)$ face of $MnCO_3$ is evident (Duckworth and Martin, 2003). The surface is subsequently exposed to oxygen-saturated solution at pH = 6.0 (Figs. 5B–D) and pH = 9.9 (Fig. 5E). In 5B after 165 min, a 2 nm discontinuous flat layer initiating from several islands grows over the terrace region. Earlier micrographs at 30 and 135 min (5C and 5D) show in more detail the time-dependent growth of the layer. The discontinuous layer does not grow over pits. Growth of this tabular precipitate also occurs preferentially along the crystallographic a-axis. Images 5C and 5D occur within a scan field (cf. debris in Fig. 5B), but an inspection of the image beyond the field shows the same basic morphologic features. This tabular precipitate occurs for 5.8 < pH < 7.7.

In 5E, which is captured after 2 h of exposure to O_2(aq) at pH = 9.9, the surface is covered with a patchy layer of flattened hillocks, which are 10–25 nm high by 500–1000 nm across. They have an apparent contact angle of 4 ± 2°. These contact angles are possibly a convolution of the AFM tip with the hillock (Westra et al., 1993). Nevertheless, they remain useful for comparison of the hillock morphologies occurring on $FeCO_3$ and $MnCO_3$. Images with hillocks are characteristic of pH > 7.7 under oxic conditions. The initial surface for 5E (not shown) is similar to 5A. Figure 2B shows a large decrease in the dissolution rate concurrent with the AFM imaging (pH > 7.7).

To aid in the identification of precipitates observed in the AFM images, XPS O 1s spectra are recorded (Fig. 6). Our approach is to record the spectra for several known minerals to determine characteristic peaks for oxygen speciated as O^{2-}, OH^-, and CO_3^{2-} and then to use these assigned peaks to interpret the spectra recorded for precipitates. To determine the characteristic peaks of the oxygen in CO_3^{2-}, reference spectra are collected for unreacted $FeCO_3$ and $MnCO_3$. Spectra for $FeCO_3$ (6A) and $MnCO_3$ (6B) both have a major peak centered at 532.3 and 532.2 eV, respectively. This binding energy is similar to that reported for oxygen in CO_3^{2-}, e.g., $BaCO_3$ at 531.2 eV, $SrCO_3$ at 531.5 eV, and $CaCO_3$ at 531.6 eV (Sosulnikov and Teterin, 1992). Stipp and Hochella (1991) report $CaCO_3$ at 531.9 eV. The small peak located at 530.1 eV in the spectrum of $MnCO_3$ may be due to oxygen or hydroxide groups associated with adventitious carbon sorbed to the mineral sur-

face. To determine the position of the O^{2-} peak, spectra are collected for hematite and pyrolusite. Spectra for the oxides have a major peak at 530.2 eV for α-Fe_2O_3 (6C) and 529.4 eV for γ-MnO_2 (6D). These binding energies are similar to those reported in literature for α-Fe_2O_3 (530 eV) (Junta and Hochella, 1994; Ding et al., 2000) and MnO (529.1 eV) (Junta and Hochella, 1994). The full width at half maxium (FWHM) for these is 1.3–1.6, which is slightly lower than the range of 1.9–2.1 reported by Junta and Hochella (1994).

To determine the position of the OH^- peak, spectra are collected for γ-FeOOH and γ-MnOOH. The FWHM for these peaks is 3.0–3.5 eV, suggesting that the peak is a convolution of smaller peaks. For γ-FeOOH (6E), the broad peak is decomposed into two smaller peaks: an O^{2-} peak at 530.0 eV and an OH^- peak at 531.9 eV, separated by 1.9 eV. This separation is slightly larger than the 1.4 eV separation reported in the literature (Junta and Hochella, 1994; Ding et al., 2000). Similar results are apparent for γ-MnOOH (6F): an O^{2-} peak at 529.5 eV and an OH^- peak at 530.9 (1.4 eV higher). Their separation agrees well with the literature value of 1.4 eV (Junta and Hochella, 1994).

An XPS spectrum of a $FeCO_3$ sample exposed to O_2(aq) at pH = 9.4 for 30 h is shown in Figure 6G. A sharp peak (FWHM = 1.5 eV) is evident at 531.9 eV, which is indicative of OH^-. Spectra (not shown) of similarly treated samples at pH = 9.2 have the same peak. The peak position at 531.8 eV implicates the formation of an iron hydroxide, either $Fe(OH)_2$ or $Fe(OH)_3$. For reasons discussed later, we believe the precipitate is $Fe(OH)_3$ (ferrihydrite).

An XPS O 1s spectrum of $MnCO_3$ exposed to O_2(aq) at pH = 7.7 for 2 h is shown in Figure 6H. The spectrum contains two peaks, located at 528.4 and 532.2 eV. These peaks respectively correspond to the O^{2-} and CO_3^{2-} peaks found in the mineral standards. The FWHM of the oxide peak is 1.9 eV, consistent with the with a single peak. This observation suggests the formation of an oxide layer such as MnO, Mn_2O_3, or MnO_2.

An XPS O 1s spectrum of $MnCO_3$ exposed to O_2(aq) at pH = 10 for 2 h is shown in Figure 6I. One broad peak (FWHM = 3.0 eV) is present. Spectral decomposition finds two peaks separated by 1.4 eV (529.1 eV and 530.5 eV). The positions and intensities of these peaks, when compared to the reference spectra, indicate the formation of an oxyhydroxide (viz. a $Mn_xO_y(OH)_y$ such as MnOOH). The slight increase of the O^{2-} peak relative to the OH^- peak, as compared to the reference minerals, may indicate co-precipitation of an oxide such as MnO, Mn_2O_3, or MnO_2 as a minor phase.

4. DISCUSSION

This section is organized as follows. Section 4.1 discusses chemical and physical aspects of the dissolution of $FeCO_3$ and $MnCO_3$ under anoxic conditions. Section 4.2 addresses the effects of O_2 on dissolution. Section 4.3 presents the conclusions drawn from the study.

4.1. Dissolution under Anoxic Conditions

4.1.1. Far from Equilibrium

Analysis of the dissolution kinetics for the pH, Fe_T, and Mn_T conditions of our work is simplified by establishing that the $FeCO_3$ and $MnCO_3$ solubility equilibria are deeply undersatu-
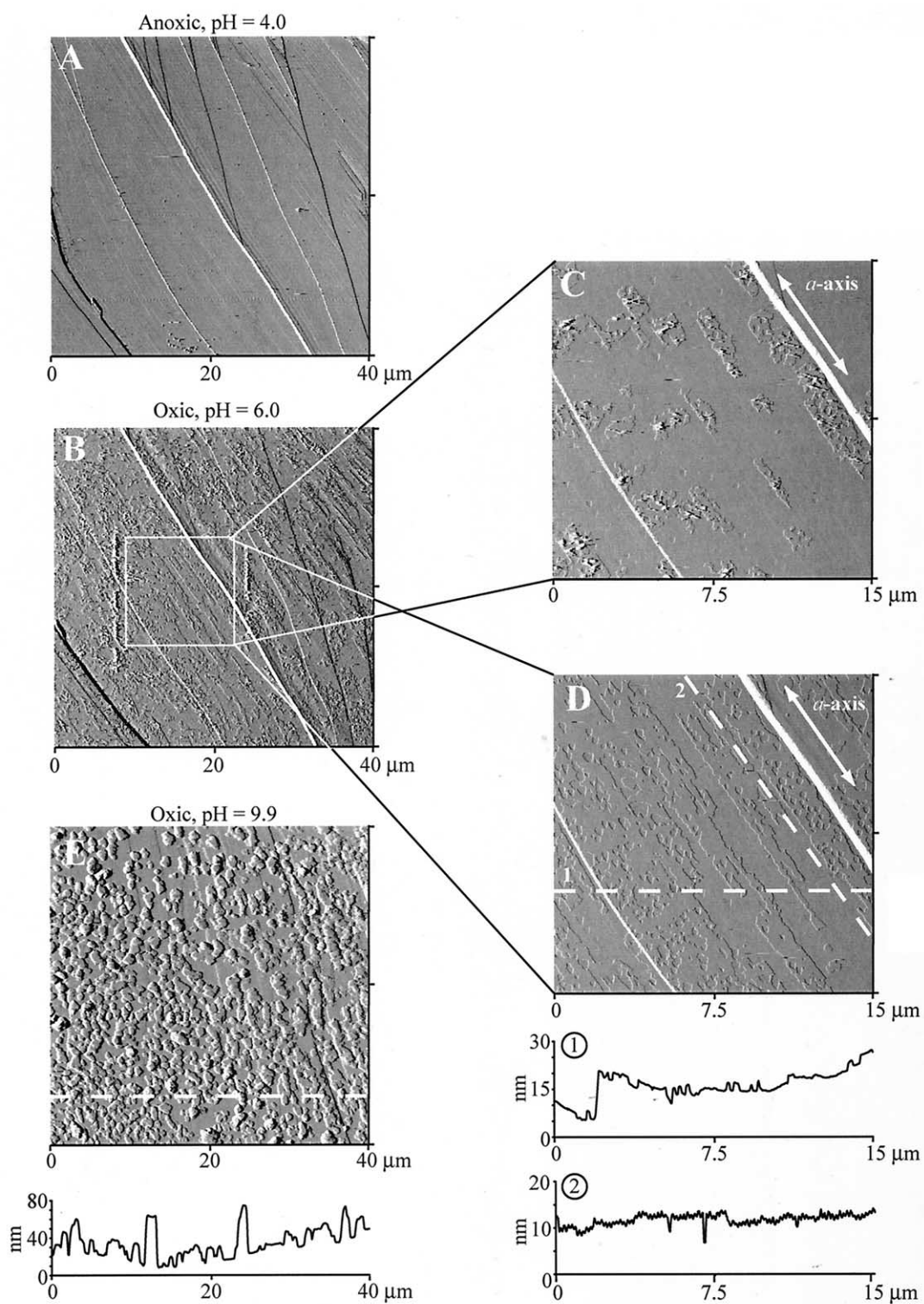
Fig. 5. AFM deflection mode micrographs and height mode cross sections showing the effect of O_2 at pH = 6.0 and 9.9 on the (10$\bar{1}$4) face of $MnCO_3$. (A) Anoxic solution at pH = 4.6. (B) A 2 nm discontinuous layer grows over the terrace region following exposure to oxygen-saturated solution at pH = 6.0 for 165 min. Earlier micrographs at 30 and 135 min (C and D) show in more detail the time-dependent growth of the layer. (E) Following exposure to O_2 at pH = 9.9 for 120 min, the surface is covered with a patchy layer of hillocks 20–25 nm high by 1000–2000 nm diameter.
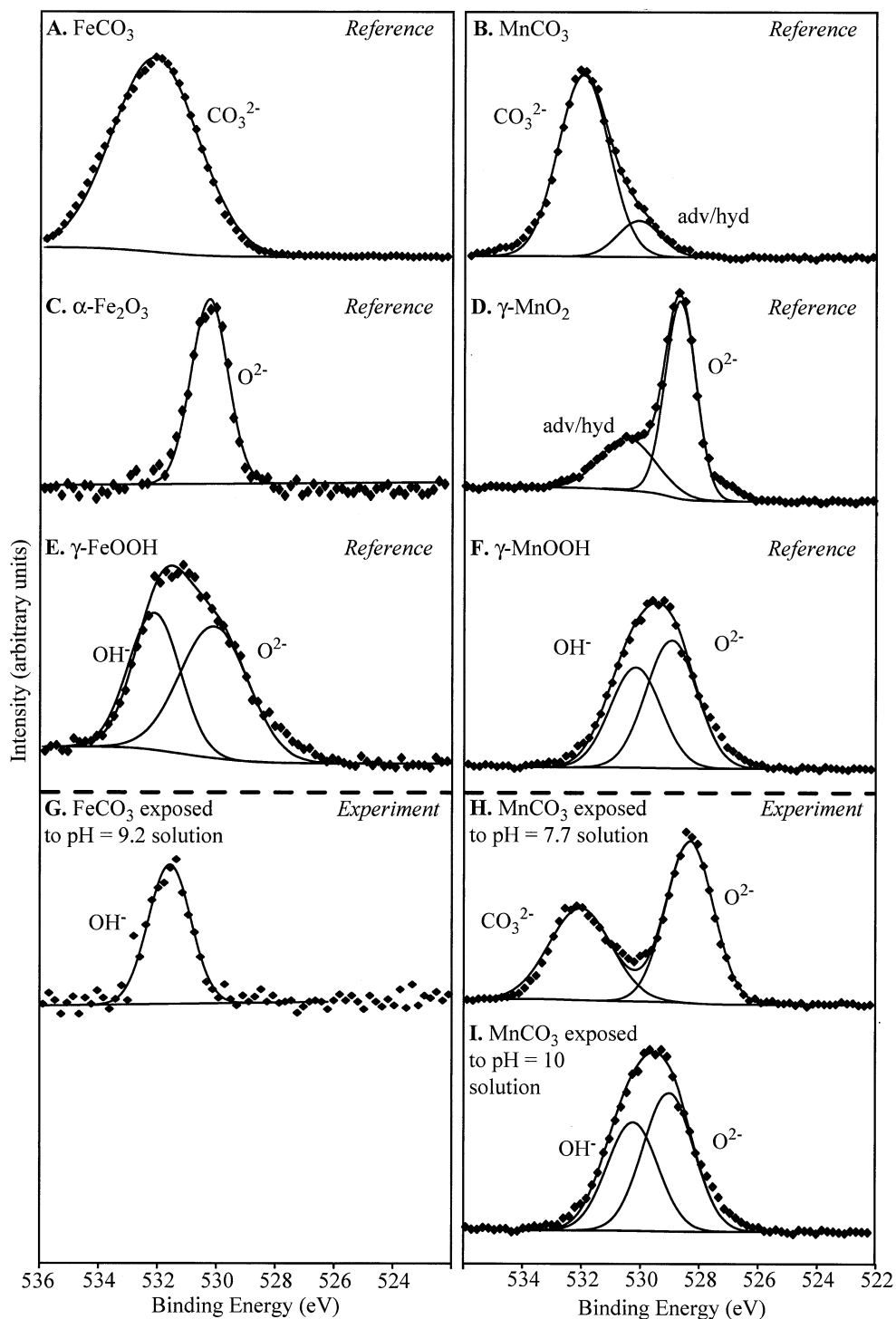
Fig. 6. O 1s XPS spectra. Spectra of iron and manganese minerals are respectively shown in the left-hand and right-hand columns. Lines show gaussian peak fits to the data.

rated under anoxic conditions. The solubility limits of $FeCO_3$ (line 2, Fig. 7A) and $MnCO_3$ (line 3, Fig. 7B) are shown. Fe_T measured in the anoxic experiments is a factor of 10^4 lower than the calculated $FeCO_3$ solubility (Fig. 7A). This relationship also holds for Mn_T with respect to $MnCO_3$ solubility (Fig.

7B). $Fe(OH)_2(s)$ and $Mn(OH)_2(s)$ are also undersaturated for the range of our experimental conditions (not shown). Under anoxic conditions the studied systems are thus far from equilibrium, and dissolution is strongly thermodynamically favorable.
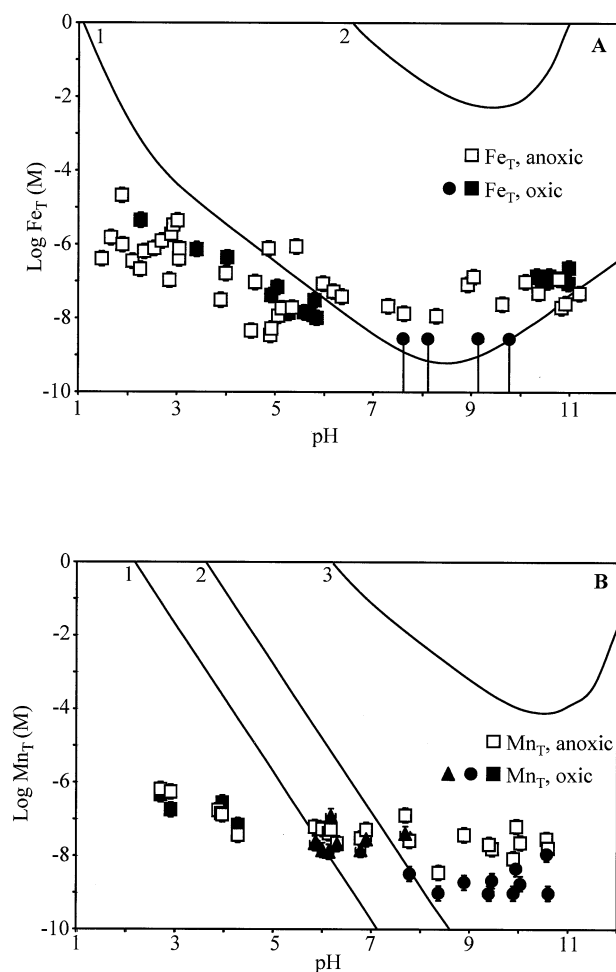
Fig. 7. Thermodynamic calculations useful for rationalizing experimental observations. (A) The calculated solubilities of ferrihydrite (line 1) and siderite (line 2) compared to experimental measurements of Fe_T. Key: Fe_T under anoxic conditions ($\square$) and Fe_T under oxic conditions when hillocks precipitate ($\bullet$) and when they do not ($\blacksquare$). (B) The calculated solubilities of bixbyite (line 1), feitknechtite (line 2), and rhodochrosite (line 3) compared to experimental measurements of Mn_T. Key: Mn_T under anoxic conditions ($\square$) and Mn_T under oxic conditions without precipitation ($\blacksquare$), with tabular precipitates ($\blacktriangle$), and with hillock precipitates ($\bullet$). For these calculations, $C_T = 10^{-6}$ M. Variance in q and A accounts for the apparent variance in Fe_T and Mn_T shown in Figures 7A,B (cf. Eqn. 1 and tighter correlation in R shown in Figs. 2A,B).

4.1.2. Mechanistic Kinetic Equations following from Macroscopic Observations

Far from equilibrium, metal carbonate dissolution rates are accurately reduced to the equations of mechanistic models (Busenberg and Plummer, 1986; Chou et al., 1989; Dresel, 1989; Duckworth and Martin, 2003). Mechanistic models are so named because they quantitatively relate dissolution rates to the aqueous concentrations of species purported to be involved in the rate-determining step of the dissolution mechanism. Our dissolution data for $FeCO_3$ and $MnCO_3$ can be explained when dissolution occurs by two parallel reactions, as follows (Busenberg and Plummer, 1986; Chou et al., 1989; Dresel, 1989; Duckworth and Martin, 2003):

$$MCO_3(s) + H^+ \rightarrow M^{2+} + HCO_3^- \quad (2)$$

$$MCO_3(s) + H_2O \rightarrow M^{2+} + HCO_3^- + OH^- \quad (3)$$
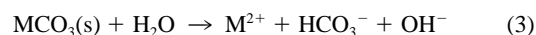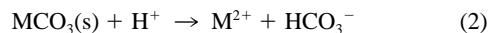
Eqns. 2 and 3 show a proton-promoted reaction, which is dominant at low pH, and a water hydrolysis reaction, which is dominant at neutral and alkaline pH.

To obtain kinetic parameters for the $FeCO_3$ mechanistic model, we optimize the least-squares fit of a power law in the concentrations of protons and water ($[H_2O] \equiv 1$) to the $FeCO_3$ anoxic rate data, as follows:

$$R_{MM}^{Fe}(mol\ m^{-2}\ s^{-1}) = 10^{-4.60}[H^+]^{0.75} + 10^{-8.65}[H_2O] \quad (4)$$

The mechanistic model dissolution rate (R_{MM}^{Fe}) is shown as the solid line in Figure 2A. The order of the reaction (0.75) and the rate coefficient ($10^{-4.60}$ $mol^{0.25}$ m^{-2} $L^{0.75}$ s^{-1}) for the acidic pathway agree well with the parameters (0.75, $10^{-4.42}$) obtained by Dresel (1989) for $0 < pH < 6$. There is also good agreement with the dissolution rates reported by Pokrovsky and Schott (2002) for $5 < pH < 8$ for aqueous $FeCO_3$ particulate suspensions. However, for $pH > 8$ Pokrovsky and Schott report a decrease in dissolution rate, which is not observed in our study, perhaps because we employ a single ($10\bar{1}4$) surface rather than particulates.

Application of the mechanistic model to the $MnCO_3$ anoxic rate data yields (Duckworth and Martin, 2003):

$$R_{MM}^{Mn}(mol\ m^{-2}\ s^{-1}) = 10^{-4.93}[H^+]^{0.5} + 10^{-8.45}[H_2O] \quad (5)$$

R_{MM}^{Mn} is shown as the solid line in Figure 2B. These dissolution rates agree well with those reported for synthetic powders for $pH < 8$ (Pokrovsky and Schott, 2002). At higher pH, however, the reported rates are slightly slower than our observed dissolution rates.

The mechanistic models presented here perform well for $pH > 3$. However, the models overpredict the dissolution rate for $pH < 3$ for both $FeCO_3$ and $MnCO_3$. A mechanistic model does not explicitly include a description of microscopic physical and chemical mechanisms active on the surface. A more detailed molecular chemical description is embodied in the surface complexation modeling approach. Surface complexation modeling of carbonates indicates that the difference between R_{MM} and the observations at $pH < 3$ is consistent with surface saturation of active chemical groups (Pokrovsky and Schott, 1999; Pokrovsky and Schott, 2002; Duckworth and Martin, 2003).

Because mechanistic models are frequently applied to $CaCO_3$ (Busenberg and Plummer, 1986; Chou et al., 1989), an important difference in interpretation for $FeCO_3$ and $MnCO_3$ should be emphasized. For $CaCO_3$ at $pH < 4$, $R_{MM}^{Ca} = 10^{-1.06}[H^+]^1$ and the interpretation is that the intrinsic chemical rate could be faster but not realized due to mass-transport kinetics limited for $pH < 4$: the overall rate is limited by proton flux from bulk solution through a quiescent boundary layer at the surface (Bosenberg and Plummer, 1986; Sjoberg and Rickard, 1984). In the case of $FeCO_3$ and $MnCO_3$, due to the slower dissolution rates, the requisite proton flux through the boundary layer is greatly diminished, and pH near the surface is essentially the same as in bulk. There is no mass transport limitation from proton flux, and the dissolution rate at low pH remains surface-controlled for $FeCO_3$ and $MnCO_3$. This fact is verified

by our conducting studies at several flow rates without observing changes in the dissolution behavior.

4.1.3. Microscopic Observations of Pit Formation and Step Retreat

The physical mechanism of dissolution of the ($10\bar{1}4$) face of the isostructural calcite family minerals, including $FeCO_3$ and $MnCO_3$, is the formation and expansion of regular rhombohedral pits (e.g., Fig. 3) (Hillner et al., 1992; MacInnis and Brantley, 1992; Liang et al., 1996a; Liang et al., 1996b; Liang and Baer, 1997; Teng and Dove, 1997; Jordan and Rammensee, 1998; Jordan et al., 2001; Higgins et al., 2002; Duckworth and Martin, 2003). For $FeCO_3$, we typically observe deep pits with pointed bottoms (cf. inset cross sections in Fig. 3). This morphology is attributed to pit formation at a screw dislocation (MacInnis and Brantley, 1992). For $MnCO_3$, typical pits are shallow and flat bottomed, arising from groups of point defects (MacInnis and Brantley, 1992). On both $FeCO_3$ and $MnCO_3$, atypical and isolated pits of variable morphology are also sometimes observed. Due to their relatively infrequent occurrence and unique morphologies, these pits are excluded in our present analysis.

4.2. Effects of Molecular Oxygen

Molecular oxygen strongly influences the rates and mechanisms of $FeCO_3$ and $MnCO_3$ dissolution. Under oxic conditions at neutral to mildly alkaline pH, oxidation of Fe^{2+} and Mn^{2+} ions results in the formation of (hydr)oxide precipitates. Oxygen also affects the dissolution rate, reducing (e.g., $MnCO_3$ for pH > 7.7 and $FeCO_3$ 6 < pH < 10.3) or increasing (e.g., $FeCO_3$ pH > 10.3) R_{ox} as compared to R_{an}.

4.2.1. Chemical Composition of Precipitates

O 1s XPS is utilized to characterize the chemical composition and speciation of the precipitates. Based on data shown in Figure 6G, we conclude the precipitate observed on $FeCO_3$ for 6 < pH < 10.3 is a hydroxide ($Fe_x(OH)_y$). Based on the spectra shown in Figures 6H and 6I, we identify the precipitate on $MnCO_3$ as an oxide (Mn_xO_y) for 5.8 < pH < 7.7 and an oxyhydroxide ($Mn_xO_y(OH)_y$) for pH > 7.7.

Previous studies have used the Fe 2p and Mn 2p spectral region to identify the oxidation state of the precipitates (Ding et al., 2000; Jun and Martin, 2002). However, the spread in the binding energies for Fe^{II}/Fe^{III} and for $Mn^{II}/Mn^{III}/Mn^{IV}$ is only a few eV so that their discrimination is difficult (Junta and Hochella, 1994). Moreover, in our studies we have an interfering signal from the underlying divalent mineral. Hence, due to a poor signal-to-noise ratio we are unable to determine the oxidation state of the precipitate from the Fe and Mn energy regions.

To complement the XPS observations, we employ thermodynamic calculations to constrain the pool of plausible precipitates. Figure 8A shows the saturation ratios of iron (hydr)oxides under our experimental conditions when precipitation is observed (e.g., Fe_T = 10 nM, P_{O2} = 1 atm). For 6.4 < pH < 10.3, S > 1 for ferrihydrite ($Fe(OH)_3$, line 4). AFM images show the precipitate occurs over this same pH range (Fig. 4B),
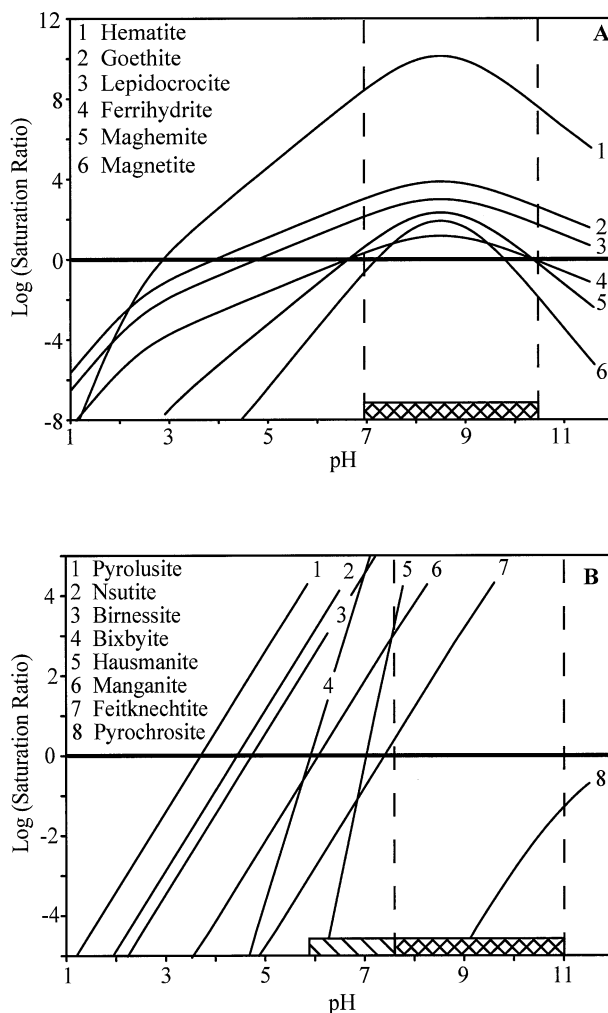

Fig. 8. Thermodynamic calculations useful in the identification of surface precipitates. (A) The saturation ratio for iron minerals shown as a function of pH under experimental conditions. (B) As in A but for manganese minerals. The dashed lines indicate pH ranges showing decreased dissolution rates under oxic conditions as compared to the corresponding anoxic conditions (cf. Fig. 2). Key: single-hashed when tabular precipitate observed in this pH range and double-hashed when hillock precipitate observed. Conditions for calculations: Fe_T = 10 nM, Mn_T = 30 nM, P_{O2} = 1 atm. (Line 4 in Fig. 8A shows understauration for pH > 10 while the data points in Fig. 7A show superaturation for pH > 10 under oxic conditions. Fig. 8A is drawn for Fe_T = 10 nM while Fig. 7A employs the measured Fe_T values.)

the XPS data indicate an iron hydroxide forms, R_{ox} < R_{an} in this pH range, and $Fe(OH)_2$ is undersaturated: we conclude that the precipitate is ferrihydrite. Ferrihydrite is also the oxidation product of $FeCO_3$ in field studies (Postma, 1983) and forms during rapid oxidation of ferrous iron (Cornell and Schwertmann, 1996). Although Figure 8A also shows supersaturation with respect to hematite (α-Fe_2O_3), goethite (α-FeOOH), lepidocrocite (γ-FeOOH), maghemite (γ-Fe_2O_3), and magnetite (Fe_3O_4), no O^{2-} peak is seen in the XPS spectrum (6G), indicating that these minerals do not form in our experiment.

Figure 8B shows the saturation ratios for manganese hydroxides under our experimental conditions when precipitation is

observed (e.g., $Mn_T = 30$ nM, $P_{O_2} = 1$ atm). The calculations (line 4) show $S > 1$ for bixbyite (Mn_2O_3) at the same pH (viz. 5.8) at which the tabular precipitate occurs (Fig. 5D). Although Figure 8B also shows supersaturation to several oxide phases over the entire pH range, including birnessite (δ-MnO_2), pyrolusite (β-MnO_2), and nsutite (γ-MnO_2), Mn^{IV}-oxide phases do not occur as initial precipitates from Mn^{2+} solutions exposed to O_2. Rather, they form over long time periods by disproportionation of Mn^{III}-containing phases (Hem, 1978). Based on these observations and the XPS identification of the precipitate as an oxide, we believe the tabular precipitate is bixbyite.

For pH > 7.7, a hillock precipitate forms (Fig. 5E) and $R_{ox} < R_{an}$ (Fig. 2B). Thermodynamic calculations show that feitknechtite (β-FeOOH) supersaturation (line 7, Fig. 8B) coincides with the appearance of the hillock precipitates. The XPS data also implicate an oxyhydroxide precipitate. Furthermore, an oxyhydroxide precipitate is consistent with literature reports of feitknechtite precipitation on hematite, goethite, and albite for 7.8 < pH < 8.7 (Junta and Hochella, 1994; Junta et al., 1997). Feitknechtite is also an intermediate phase in the growth of manganite and Mn^{IV}-oxides (Hem et al., 1982). Even so, Figure 8B also shows manganite (γ-MnOOH) is supersaturated ($S = 1000$ at pH = 8) (line 6), and we could find no thermodynamic data for groutite (α-MnOOH). We therefore tentatively identify the hillock precipitate as feitknechtite with the caveat that other MnOOH polymorphs are not conclusively ruled out.

4.2.2. Location and Morphology of Precipitates

Under oxygen-saturated conditions for 7.5 < pH < 10.3, hillock $Fe(OH)_3$(s) precipitates form preferentially at steps on $FeCO_3$ (Fig. 4B), which may be explained by two alternative mechanisms. In the first mechanism, ferrous auto-oxidation occurs in homogeneous solution to yield $Fe(OH)_3$(aq) monomers. Homogeneous oxidation rates are rapid for pH > 7.5 (Sung and Morgan, 1980), and ferrous carbonate complexes accelerate the rate (King, 1998). The $Fe(OH)_3$(aq) monomers diffuse to the surface terrace where they adsorb weakly. Surface diffusion is rapid, and the monomers come to rest at morphologic features on the surface, such as steps, where polymerization is favorable. The net observable of the processes is preferential formation of hillocks at steps (e.g., Fig. 4B). Detailed descriptions of this mechanism are offered by Markov (1995) or Lasaga (1998).

An alternative mechanism is heterogeneous oxidation (Wehrli, 1990). Iron (III) oxide surfaces and carbonate minerals promote the oxidation of Fe^{2+} at circumneutral pH (Tamura et al., 1976; Mettler and Von Gunten, 2002). If heterogeneous reaction rates are faster at steps than terrace regions of $FeCO_3$ and further if reaction rates on the surface of freshly formed precipitate are even faster, then precipitation followed by hillock growth occurs at steps (e.g., Fig. 4B). Junta and Hochella (1994) formulate a model description of these processes for Mn^{2+} oxidation on albite. Surface complexation modeling calculates a maximum for adsorbed Fe^{2+} on siderite in the range 7.5 < pH < 10.3 (Van Cappellen et al., 1993), further suggesting that sufficient Fe^{2+} is adsorbed for heterogeneous oxidation to be significant.

In contrast to the single precipitate observed for $FeCO_3$, two distinct precipitates of differing chemistry and morphology form on $MnCO_3$, one for 5.8 < pH < 7.7 and one for pH > 7.7 (Figs. 5D,E). Unlike Fe^{2+} auto-oxidation for which homogeneous and heterogeneous pathways are both rapid, heterogeneous rates are more rapid than homogenous rates for Mn^{2+}, at least for pH < 10 (Sung and Morgan, 1981; Diem and Stumm, 1984; Davies and Morgan, 1989; Junta and Hochella, 1994; Junta et al., 1997; Jun and Martin, 2002).

The MnOOH precipitates occurring for pH > 7.7 are observed as flattened hillocks on the terrace without apparent preference for steps or kinks (Fig. 5E). The behavior apparent for the MnOOH precipitate is in direct contrast to that shown for $Fe(OH)_3$(s) in Figure 4B. In both cases, hillocks form but do so with and without surface site specificity, respectively, for $Fe(OH)_3$(s) and MnOOH(s). The model of Junta and Hochella (1994) predicts specificity when heterogeneous nucleation rates at steps and on fresh precipitate exceed those of terrace regions, while nonspecificity holds otherwise. For hillocks to develop without specificity (cf. Fig. 5E), monomers should diffuse more slowly to steps than they accumulate from surface attachment accompanying precipitation.

The Mn_2O_3 precipitate forms a tabular morphology for 5.8 < pH < 7.7, with preferential growth along the a-axis of the substrate. The morphology and growth characteristics suggest oxidation and precipitation occur on terraces as opposed to steps (cf. Figs. 5C,D). We conclude there is favorable epitaxial interaction between the $(10\bar{1}4)$ face of $MnCO_3$ and the Mn_2O_3 precipitate, and that this strong interaction leads to crystallographic control over precipitate growth. Lattice misfit f is the an important factor governing epitaxial growth (Markov, 1995) and is given by $f = (b - a)/a$ where a and b are atomic spacings of the substrate and the precipitate, respectively. Efficient epitaxial growth is generally observed for $< |15\%|$. We calculate $f = 8.5\%$ from Mn-O distance of 2.003 Å for Mn_2O_3 (Geller, 1971) and of 2.190 Å for $MnCO_3$ (Effenberger et al., 1981). The atomic spacings thus suggest epitaxial growth is possible, although a more thorough analysis of the crystallographic fit requires treatment of specific abutting crystal faces and the atomic positions of relaxed surfaces.

4.2.3. Relationships between Microscopic Observations and Apparent Dissolution Rates

To link the microscopic effects of O_2(aq) to changes in macroscopic dissolution rates R, we regard R as an intrinsic dissolution rate less a precipitation rate. The intrinsic dissolution rate, taken as equal to R_{an} in our treatment, is constant for a fixed pH, and any decrease is understood to arise from an increase in precipitation rate. This linear additive approach is used by Busenberg and Plummer (1986) in a general model of $CaCO_3$ dissolution, including the effects of Ca^{2+}, HCO_3^-, and H_2CO_3. A more detailed approach than offered by us would attempt to explore the effects on the intrinsic dissolution rate, such as possible decreases arising from adsorption of oxidized Fe^{3+} and Mn^{3+} monomers at dissolution active steps (Davis et al., 2000; Lea et al., 2001) or poisoning by formation of a thick coating of a nonreactive reaction product. Our simplified approach, which is adopted for the interpretation of our data, is appropriate to the level of information we have.

According to the approach just described, molecular oxygen

affects R through precipitation of (hydr)oxide phases. A simple test of the accuracy of this description is that O_2(aq) should decrease R only under conditions for which (hydr)oxide precipitation is thermodynamically favorable. Based upon our conclusions in §4.2.1, the relevant solids for analysis include ferrihydrite, bixbyite, and feitknechtite. The solid symbols in Figure 7A show the observed Fe_T in oxic dissolution experiments as compared to the calculated Fe_T solubility of ferrihydrite (line 1). For acidic pH, ferrihydrite is undersaturated, and O_2 does not affect R (i.e., $R_{ox} = R_{an}$) (Fig. 2A). The dissolution kinetics are far from equilibrium, and the apparent and intrinsic dissolution rates are taken as equal. The results are consistent with the absence of precipitates in the AFM images.
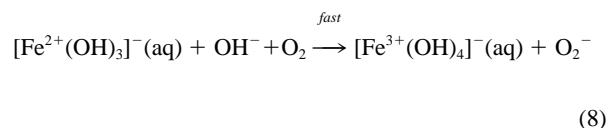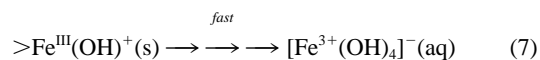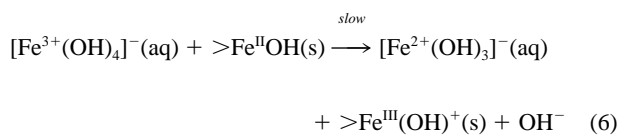
For $7 < $ pH $ < 10.3$, though Fe_T is below our detection limit, this limit is above the calculated solubility of ferrihydrite (Fig. 7, line 1), which is consistent with the precipitate observed in the AFM images and also the effect of O_2 on reducing R (i.e., $R_{ox} < R_{an}$) (Fig. 2A). Although the dissolution kinetics for $FeCO_3$ are far from equilibrium, the $Fe(OH)_3$ precipitation rate nearly balances the $FeCO_3$ intrinsic dissolution rate. The apparent dissolution rate is then slow, and the overall rate of material removal could be solubility-controlled by ferrihydrite if its precipitation rate fully equals the $FeCO_3$ dissolution rate.

We follow a similar analysis to elucidate the effect of O_2 on $MnCO_3$ dissolution. Figure 7B shows Mn_T in equilibrium with bixbyite (line 1) and feitknechtite (line 2) as well as Mn_T observations from the oxic experiments (solid symbols). For pH $ < 6$, bixbyite and feitknechtite are both undersaturated, no precipitation is observed in the AFM images, the dissolution kinetics are far from equilibrium, and O_2 does not affect dissolution (Fig. 2B). For pH $ > 6$, as compared to solution conditions, bixbyite and feitknechtite are supersaturated, and precipitation is observed in the AFM images. While $MnCO_3$ dissolution kinetics remain far from equilibrium ($S \ll 1$), the growing bixbyite and feitknechtite crystals are also far from equilibrium in being highly supersaturated ($S \gg 1$). Although as expected O_2 reduces R when the hillock precipitate is observed (pH $ > 7.7$), formation of the tabular precipitate ($5.8 < $ pH $ < 7.7$) does not affect R (Fig. 2B). The selective avoidance of pits by the advancing tabular precipitate (Fig. 5D) rationalizes the lack of an effect of the precipitation on the intrinsic dissolution rate because $MnCO_3$ dissolution is most active at pit edges. Alternatively, because the precipitate is only a thin layer, the precipitation rate may simply be too slow to reduce noticeably the relatively fast apparent dissolution rate.

4.2.4. Electron Transfer to Surficial Iron

For pH $ > 10$ the $FeCO_3$ dissolution rate increases rapidly in the presence of O_2 and exceeds R_{an} (Fig. 2A). Moreover, the precipitate observed for $7 < $ pH $ < 10.3$ in the AFM images does not occur at higher pH, even after exposure in one trial extending to 21 h at pH $ = 10.6$. The absence of the precipitate is rationalized by Figure 8A showing that ferrihydrite formation is unfavorable at high pH. However, an explanation for $R_{ox} > R_{an}$ requires formulation of a novel hypothesis. Based on observations reported in the literature for pyrite (Moses et al., 1987; Moses and Herman, 1991) and aqueous iron chemistry (King, 1998; Rosso and Morgan, 2002), we propose two possible electron transfer mechanisms.

In mechanism one, $[Fe^{3+}(OH)_4]^-$(aq) is a rapid electron shuttle. The proposed mechanism is as follows:

$$[Fe^{3+}(OH)_4]^-(aq) + >Fe^{II}OH(s) \xrightarrow{slow} [Fe^{2+}(OH)_3]^-(aq)$$

$$+ >Fe^{III}(OH)^+(s) + OH^- \quad (6)$$

$$>Fe^{III}(OH)^+(s) \xrightarrow{fast} \longrightarrow \longrightarrow [Fe^{3+}(OH)_4]^-(aq) \quad (7)$$

$$[Fe^{2+}(OH)_3]^-(aq) + OH^- + O_2 \xrightarrow{fast} [Fe^{3+}(OH)_4]^-(aq) + O_2^-$$

$$(8)$$

In Eqn. 6, $[Fe^{3+}(OH)_4]^-$(aq) scavenges an electron from surficial $>Fe^{II}OH$. The oxidized surface species, which is a poor crystallographic fit for the lattice, dissolves from the mineral matrix (Eqn. 7). The reduced $[Fe^{2+}(OH)_3]^-$(aq) returns to bulk solution and is recycled to $[Fe^{3+}(OH)_4]^-$(aq) by dissolved O_2 (Eqn. 8). The net result of this cycle is:

$$>Fe^{II}OH(s) + O_2 \rightarrow [Fe^{3+}(OH)_4]^-(aq) + O_2^- \quad (9)$$
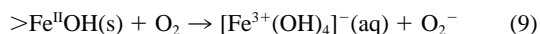
Charge balance, which is not explicitly shown in Eqn. 7 and 9, involves protonation and deprotonation of surface sites accompanying release of Fe(III) from the lattice as well as aqueous speciation in homogeneous solution among hydrolysis species.

The reaction sequence (Eqn. 6–8) and the species involved are plausible. The dominant speciation of Fe_T is ferric ion in our experiments at pH $ > 9$ due to rapid oxidation kinetics (Sung and Morgan, 1980). Moreover, for pH $ > 9$ due to rapid hydrolysis, Fe_T is dominantly speciated as $[Fe^{3+}(OH)_4]^-$(aq) (Stumm and Morgan, 1996). The electron transfer lability of iron hydrolysis species rapidly increases with n in $Fe^{z+}(OH)_n^{z-n}$, at least for electron exchange reactions in the series $n = 0$, 1, and 2 (Rosso and Morgan, 2002). The species $[Fe^{3+}(OH)_4]^-$ is thus plausibly hypothesized as labile towards electron exchange with surficial $>Fe^{II}OH$ groups. A related conclusion was previously reached for pyrite (FeS_2): aqueous ferric iron promotes pyrite dissolution by shuttling electrons from solution to the mineral surface (Moses et al., 1987; Moses and Herman, 1991). At least one difference, however, is that aqueous iron oxidizes the surface anion (i.e., the sulfur) in the case of pyrite, in contrast to the Fe-Fe exchange we propose for $FeCO_3$.

In mechanism two, aqueous O_2 directly attacks $>Fe^{II}$, which is facilitated by a change in the dominant speciation from $>Fe^{II}OH_2^+$ to a more susceptible $>Fe^{II}O^-$. The pH at which speciation changes (Fig. 9B, insert) coincides with the onset pH of $R_{ox} > R_{an}$. The reaction is as follows:

$$O_2(aq) + >Fe^{II}O^-(s) \longrightarrow O_2^-(aq) + >Fe^{III}O(s) \quad (10)$$
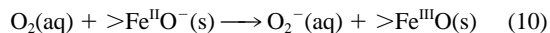
This reaction is followed by rapid dissolution (Eqns. 7 and 8).

Reaction 10 is analogous to aqueous iron oxidation chemistry, which is rapid at high pH. Our corollary hypothesis is that oxidation of $>Fe^{II}O^-$ by O_2 is more rapid than that of the protonated surface species dominant at lower pH (viz.,
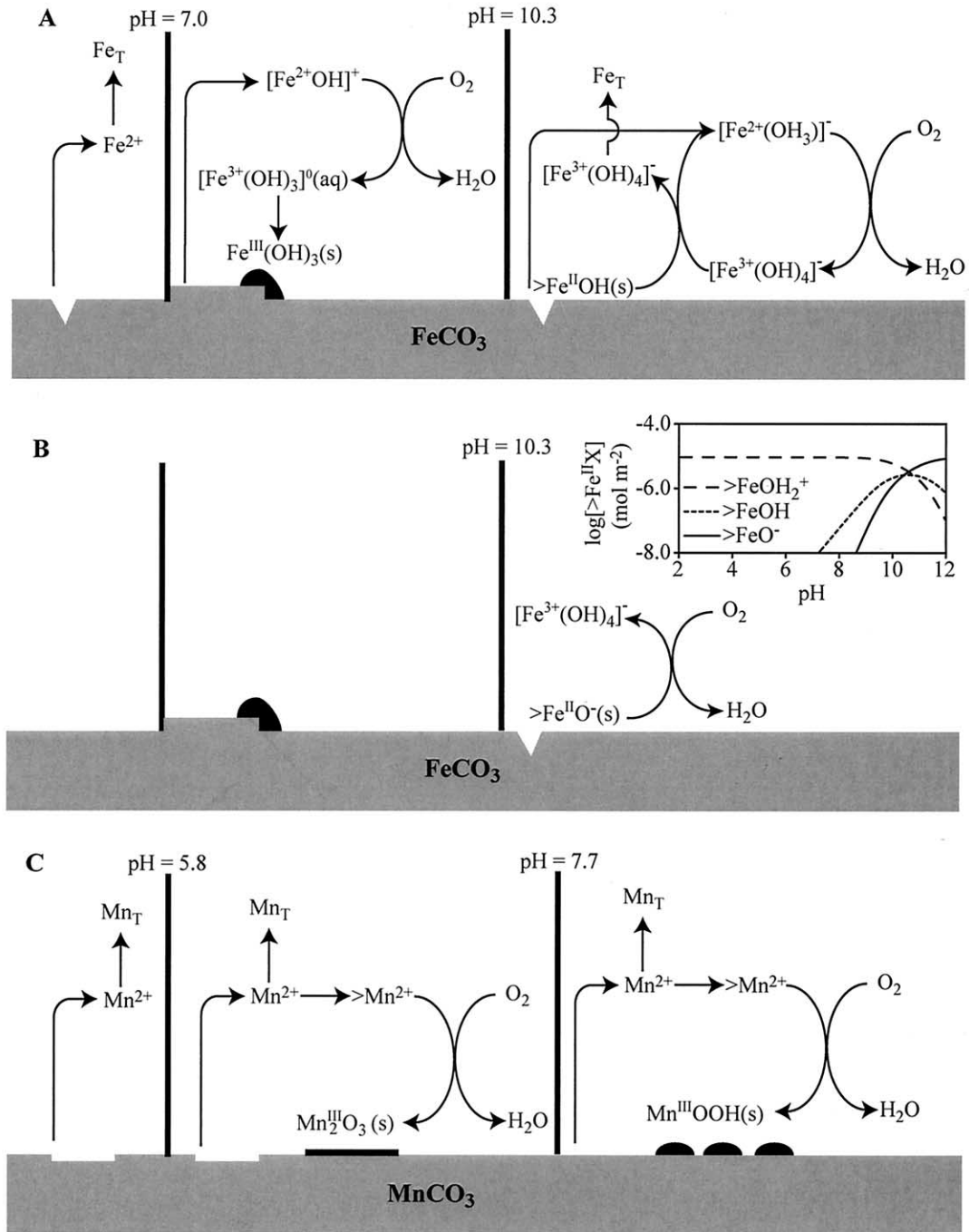
Fig. 9. Depiction of the proposed dissolution and precipitation reaction mechanisms active under oxic conditions over a range of pH regimes for (A, B) $FeCO_3$ and (C) $MnCO_3$. Under anoxic conditions, dissolution reactions at all pH values are identical to those shown for low pH oxic conditions. The aqueous speciation of Fe^{2+} and Fe^{3+} in (A) is presented in Stumm and Morgan (1996). Insert B: Fe^{II} hydroxyl speciation for experimental conditions.

$>Fe^{II}OH$ and $>Fe^{II}OH^{2+}$). Aqueous ferrous iron carbonate species (i.e., $Fe^{2+}CO_3(aq)$, $[Fe^{2+}(CO_3)_2]^{2-}(aq)$, $[Fe^{2+}HCO_3]^+(aq)$, and $[Fe^{2+}(CO_3)(OH)]^-$) are susceptible to oxidation (King, 1998), suggesting that Fe^{II} hydroxyl groups in the $FeCO_3$ surface react with $O_2(aq)$.

The proton- and water-promoted pathways (Eqns. 2 and 3) occur in parallel to the hypothesized electron transfer pathways.

However, dissolution by the electron transfer pathways (e.g., Eqns. 6–10) are more rapid in oxic solution at pH > 10.3.

5. CONCLUSIONS

Under anoxic conditions, $FeCO_3$ and $MnCO_3$ dissolve chemically by parallel proton- and water-promoted pathways and

physically by pit formation and step retreat. $FeCO_3$ and $MnCO_3$ solution concentrations are always far from equilibrium for the entire pH and P_{O2} range of the conditions of our study. The dissolution and precipitation reaction mechanisms under oxic conditions are summarized in Figure 9. Under acidic oxic conditions, dissolution occurs by the same mechanism as the corresponding anoxic case. Under oxic conditions and neutral to mildly alkaline pH, surface precipitates and $R_{ox} < R_{an}$ rate are observed for both minerals. Thermodynamic calculations rationalize the reduction in the dissolution rate: O_2 reduces R at pH values where the presence of O_2 yields saturation of (hydr)oxide solids. XPS results and thermodynamic calculations implicate $Fe(OH)_3$ as the hillock precipitate on $FeCO_3$ for $7 <$ pH < 10.3, Mn_2O_3 as the tabular precipitate on $MnCO_3$ for $5.8 <$ pH < 7.7, and $MnOOH$ as the hillocks on $MnCO_3$ for pH > 7.7. Due to a low affinity of iron ions or hydroxide monomers for the terrace region of the surface, iron hydroxide hillock precipitates form at steps on $FeCO_3$. In contrast, the lack of site specificity of the manganese oxide hillock precipitate indicates a strong affinity of manganese ions or oxide monomers for the $MnCO_3$ surface. For $FeCO_3$ at pH > 10.3, $R_{ox} > R_{an}$ due to by oxidative attack by aqueous O_2 or $[Fe^{3+}(OH_4)]^-$.

Our results show that molecular oxygen is a critical factor for quantitative treatments of the dissolution and precipitation of transition metal carbonates and (hydr)oxides for pH > 6. Because carbonate minerals occur in environments undergoing both gradual (e.g., seasonal) and abrupt (e.g., episodic) changes in pH and pE, (hydr)oxide patinas occur widely and, when they occur, regulate the release rate of transition metal micronutrients to the aqueous phase. The apparent macroscopic dissolution rate is slowed. Future work is needed to investigate the properties and persistence of the (hydr)oxide patinas in variable chemical environments.

Associate editor: U. Becker

REFERENCES

Amirbahman A., Schoenberger R., Johnson C., and Sigg L. (1998) Aqueous- and solid-phase biogeochemistry of a calcareous aquifer system downgradient from a municipal solid waste landfill (Winterthur, Switzerland). *Environ. Sci. Technol.* **32,** 1933–1940.

Barhrig B. (1985) Paleo-environment information from deep water siderite (Lake of Laach, West Germany). In *Lacustrine Petroleum Source Rocks* (eds. A. J. Fleet, K. Kelts, and M. R. Talbot), pp. 153–158. Geological Society of America.

Bruno J., Wersin P., and Stumm W. (1992) On the influence of carbonate in mineral dissolution: II. The solubility of Fe CO_3(s) at 25° C and 1 atm total pressure. *Geochim. Cosmochim. Acta* **56,** 1149–55.

Busenberg E. and Plummer L. N. (1986) A comparative study of the dissolution and crystal growth kinetics of calcite and aragonite. *U.S. Geol. Surv. Bull.* **1578,** 139–168.

Calvert S. E. and Pedersen T. F. (1996) Sedimentary geochemistry of manganese: Implications for the environment of formation of manganiferous black shales. *Econ. Geol. Bull. Soc.* **91,** 36–47.

Calvert S. E. and Price N. B. (1972) Diffusion and reaction profiles of dissolved manganese in the pore waters of marine sediments. *Earth Planet. Sci. Lett.* **16,** 245–249.

Chou L., Garrels R. M., and Wollast R. (1989) Comparative study of the kinetics and mechanisms of dissolution of carbonate minerals. *Chem. Geol.* **78,** 269–282.

Cornell R. M. and Schwertmann U. (1996) *The Iron Oxides.* VCH.

Curtis C., Pearson M., and Somogyi V. (1975) Mineralogy, chemistry, and origin of concretionary siderite sheet in the Westphalian of Yorkshire. *Mineral. Mag.* **40,** 385–393.

Davies S. and Morgan J. (1989) Manganese(II) oxidation-kinetics on metal oxide surfaces. *J. Coll. Int. Sci.* **129,** 63–77.

Davis K. J., Dove P. M., and De Yoreo J. J. (2000) The role of Mg^{2+} as an impurity in calcite growth. *Science* **290,** 724–727.

Diem D. and Stumm W. (1984) Is dissolved Mn^{2+} being oxidized by O_2 in absence of Mn-bacteria or surface catalysts? *Geochim. Cosmochim. Acta* **48,** 1571–1573.

Ding M., de Jong B. H. W. S, Roosendaal S. J., and Vredenbeg A. (2000) XPS studies on the electronic structure of bonding between solid and solutes: Adsorption of arsenate, chromate, phosphate, Pb^{2+}, and Zn^{2+} ions on amorphous black ferric oxyhydroxide. *Geochim. Cosmochim. Acta* **64,** 1209–1219.

Dresel P. E. (1989) The dissolution kinetics of siderite and its effect on acid mine drainage. Ph.D. thesis. Pennsylvania State University.

Duckworth O. W. and Martin S. T. (2003) Connections between surface complexation and geometric models of mineral dissolution investigated for rhodochrosite. *Geochim. Cosmochim. Acta* **67,** 1787–1801.

Duff M. L., Coughlin J. J., and Hunter D. B. (2002) Uranium coprecipitation with iron oxide minerals. *Geochim. Cosmochim. Acta* **66,** 3533–3549.

Effenberger H., Mereiter K., and Zemann J. (1981) Crystal structure refinements of mangesite, calcite, rhodochrosite, siderite, smithsonite, and dolomite, with discussion of some aspects of the stereochemistry of calcite type carbonates. *Zeitschr. Kristallogr.* **156,** 233–243.

Friis A. R., Davis T. A., Figueira M. M., Paquette J., and Mucci A. (2003) Influence of *Bacullus subtilis* cell walls and EDTA on calcite dissolution rates and crystal surface features. *Environ. Sci. Technol.* **37,** 2376–2383.

Geller S. (1971) Structures of α-Mn_2O_3, $(Mn_{0.983}Fe_{0.017})_2O_3$ and $(Mn_{0.37}Fe_{0.63})_2O_3$ and relation to magnetic ordering. *Acta Cryst. B* **27,** 821–828.

Harvey D. T. and Linton R. W. (1981) Chemical characterization of hydrous ferric oxides by X-ray photoelectron spectroscopy. *Anal. Chem.* **53,** 1684–1688.

Hem J. D. (1978) Redox processes at surfaces of manganese oxide and their effects on aqueous metal ions. *Chem. Geol.* **21,** 199–218.

Hem J. D., Roberson C. E., and Fournier R. B. (1982) Stability of β-$MnOOH$ and manganese oxide deposits from springwater. *Water Resour. Res.* **18,** 563–570.

Hem J. D., Lind C. J., and Roberson C. E. (1989) Coprecipitation and redox reactions of manganese oxides with copper and nickel. *Geochim. Cosmochim. Acta* **53,** 2811–2822.

Higgins S. R., Boram L., Eggleston C. M., Coles B. A., Compton R. G., and Knauss K. G. (2002) Dissolution kinetics, step and surface morphology of magnesite (104) surface in acidic solution at 60°C by atomic force microscopy under defined hydrodynamic conditions. *J. Phys. Chem.* **106,** 6696–6705.

Hillner P. E., Gratz A. J., Manne S., and Hansma P. K. (1992) Atomic-scale imaging of calcite growth and dissolution in real time. *Geology* **20,** 359–362.

Huckriede H. and Meischner D. (1996) Origin and environment of manganese-rich sediments within black shale basins. *Geochim. Cosmochim. Acta* **60,** 1399–1413.

Jenne E. (1968) Controls on Mn, Fe, Co, Ni, Cu, and Zn concentrations in soils and water: The significant role of hydrous Mn and Fe oxides. In *Trace Inorganics in Water* (ed. R. Baker), pp. 337–387. American Chemical Society.

Jensen D. L., Boddum J. V., Tjell J. L., and Christensen T. H. (2002) The solubility of rhodochrosite ($MnCO_3$) and siderite ($FeCO_3$) in anaerobic aquatic environments. *Appl. Geochem.* **17,** 503–511.

Jordan G. and Rammensee W. (1998) Dissolution rates of calcite
(10$\bar{1}$4) obtained by scanning force microscopy: Microtopography-
based dissolution kinetics on surfaces with anisotropic step veloci-
ties. *Geochim. Cosmochim. Acta* **62**, 941–947.

Jordan G., Higgins S. R., Eggleston C. M., Knauss K. G., and Schmahl
W. W. (2001) Dissolution kinetics of magnesite in acidic aqueous
solution, a hydrothermal atomic force microscopy (HAFM) study:
Step orientation and kink dynamics. *Geochim. Cosmochim. Acta* **65**,
4257–4266.

Jun Y. and Martin S. T. (2003) Microscopic observations of reductive
manganite dissolution under oxic conditions. *Environ. Sci. Technol.*
37, 2363–2370.

Junta J. L. and Hochella M. F. (1994) Manganese (II) oxidation at
mineral surfaces: A microscopic and spectroscopic study. *Geochim.
Cosmochim. Acta* **58**, 4985–4999.

Junta J. L., Hochella M. F., Jr., and Rimstidt D. (1997) Linking
microscopic and macroscopic data for heterogeneous reactions illus-
trated by oxidation of manganese (II) at mineral surfaces. *Geochim.
Cosmochim. Acta* **61**, 149–159.

Kelts K. (1998) Environments of deposition of lacustrine petroleum
source rocks: An introduction. In *Lacustrine Petroleum Source
Rocks* (eds. A. Fleet, K. Kelts, and M. Talbot), pp. 3–26. Geological
Society of America.

King D. W. (1998) Role of carbonate speciation on the oxidation rates
of Fe(II) in aqueous systems. *Environ. Sci. Technol.* **32**, 2997–3003.

Klein C. and Hurlbut J. C. S. (1993) *Manual of Mineralogy*. Wiley.

La Force M., Hansel C., and Ferdoff S. (2002) Seasonal transforma-
tions of manganese in a palustrine emergent wetland. *Soil Sci. Am. J.*
66, 1377–1389.

Lasaga A. C. (1998) *Kinetic Theory in the Earth Sciences*. Princeton
University Press.

Lea A. S., Amonette J. E., Baer D. R., Liang Y., and Colton N. G.
(2001) Microscopic effects of carbonate, manganese, and strontium
ions on calcite dissolution. *Geochim. Cosmochim. Acta* **65**, 369–379.

Li Y., Bischoff J., and Mathieu G. (1969) The migration of manganese
in the artic basin sediment. *Earth Planet. Sci. Lett.* **7**, 265–270.

Liang Y. and Baer D. R. (1997) Anisotropic dissolution at the $CaCO_3$
(10$\bar{1}$4)–water interface. *Surf. Sci.* **373**, 275–287.

Liang Y., Baer D. R., McCoy J. M., Amonette J. E., and LaFemina J. P.
(1996a) Dissolution kinetics at the calcite–water interface. *Geochim.
Cosmochim. Acta* **60**, 4883–4887.

Liang Y., Baer D. R., McCoy J. M., and LaFemina J. P. (1996b)
Interplay between step velocity and morphology during the dissolu-
tion of $CaCO_3$ surface. *J. Vac. Sci. Technol. A* **14**, 1368–1375.

MacInnis I. N. and Brantley S. L. (1992) The role of dislocations and
surface morphology in calcite dissolution. *Geochim. Cosmochim.
Acta* **56**, 1113–1126.

Markov I. (1995) *Crystal Growth for Beginners*. World Scientific.

McBride M. B. (1994) *Environmental Chemistry of Soils*. Oxford
University Press.

McIntyre N. and Zetruk D. (1975) X-ray photoelectron spectroscopic
studies of iron oxides. *Anal. Chem.* **49**, 1521–1529.

McMillan S. and Schwertmann U. (1998) Morphological and genetic
relations between siderite, calcite, and goethite in a low moor peat
from southern Germany. *Eur. J. Soil Sci.* **49**, 283–293.

Mettler S. and Von Gunten U. (2002) Reactivity of Fe(II) in the
presence of calcite and $Fe/CaCO_3$ solid-solution. *Geochim. Cosmo-
chim. Acta* **66**, A509.

Middelburg J., De Lange G., and Van Der Weijden C. (1987) Manga-
nese solubility control in marine porewaters. *Geochim. Cosmochim.
Acta* **51**, 759–763.

Morgan J. (1967) Chemical equilibria and kinetic properties of man-
ganese in natural water. In *Principles and Applications of Water
Chemistry* (eds. S. Faust and J. Hunter), pp. 561–623. Wiley.

Moses C. and Herman J. (1991) Pyrite oxidation at circumneutral pH.
Geochim. Cosmochim. Acta **55**, 471–482.

Moses C., Nordstrom D., Herman J., and Mills A. (1987) Aqueous
pyrite oxidation by dissolved oxygen and by ferric iron. *Geochim.
Cosmochim. Acta* **51**, 1561–1571.

O'Keeffe M. and Hyde B. (1996) *Crystal Structures I. Patterns and
Symmetry*. Mineralogical Society of America.

Pokrovsky O. S. and Schott J. (1999) Processes at the magnesium
bearing carbonates/solution interface. II. Kinetics and mechanisms
of magnesite dissolution. *Geochim. Cosmochim. Acta* **63**, 881–897.

Pokrovsky O. S. and Schott J. (2001) Kinetics and mechanisms of
dolomite dissolution in neutral to alkaline solutions revisited. *Am. J.
Sci.* **301**, 597–626.

Pokrovsky O. S. and Schott J. (2002) Surface chemistry and dissolution
kinetics of divalent metal carbonates. *Environ. Sci. Technol.* **36**,
426–432.

Postma D. (1977) The occurrence and chemical composition of recent
Fe-rich mixed carbonates in a river bog. *J. Sed. Petrol.* **47**, 1089–
1098.

Postma D. (1981) Formation of siderite and vivianite and the pore-
water composition of a recent bog sediment in Denmark. *Chem.
Geol.* **31**, 225–244.

Postma D. (1982) Pyrite and siderite formation in brackish and fresh-
water swamp sediments. *Am. J. Sci.* **282**, 1151–1183.

Postma D. (1983) Pyrite oxidation in swamp sediments. *J. Soil. Sci.* **34**,
163–182.

Rieutord F., Salmeron, M. (1998) Wetting properties at the submi-
crometer scale: A scanning polarization force microscopy study. *J.
Phys. Chem. B.* **102**, 3941–3944.

Rosso K. M. and Morgan J. (2002) Outer-sphere electron transfer
kinetics of metal ion oxidation by molecular oxygen. *Geochim.
Cosmochim. Acta* **66**, 4223–4233.

Schecher W. (2001) Thermochemical data used in MINEQL+ version
4.5 with comparisons to versions 4.07 and earlier. Environmental
Research Software.

Shiraki R., Rock P. A., and Casey W. H. (2000) Dissolution kinetics of
calcite in 0.1 M NaCl solution at room temperature: An atomic force
microscope study. *Aquat. Geochem.* **6**, 87–108.

Sjoberg E. and Rickard D. (1984) Calcite dissolution kinetics: Surface
speciation and the origin of the variable pH dependence. *Chem.
Geol.* **42**, 119–136.

Sosulnikov M. and Teterin Y. (1992) X-ray photoelectron studies of
Ca, Sr, Ba, and their oxides and carbonates. *J. Electron Spectrosc.
Relat. Phenom.* **59**, 111–126.

Sternbeck J. (1997) Kinetics of rhodochrosite crystal growth at 25°C:
The role of surface speciation. *Geochim. Cosmochim. Acta* **61**,
785–793.

Stipp S. L. and Hochella M. F., Jr.. (1991) Structure and bonding
environments at the calcite surface as observed with X-ray photo-
electron spectroscopy (XPS) and low energy electron diffraction
(LEED). *Geochim. Cosmochim. Acta* **55**, 1723–1736.

Stumm W. and Morgan J. J. (1996) *Aquatic Chemistry*. Wiley.

Sung W. and Morgan J. (1980) Kinetics and products of ferrous iron
oxygenation in aqueous systems. *Environ. Sci. Technol.* **14**, 561–
568.

Sung W. and Morgan J. (1981) Oxidative removal of Mn(II) from
solution catalyzed by γ-FeOOH (lepidocrocite) surface. *Geochim.
Cosmochim. Acta* **45**, 2377–2383.

Tamura H., Goto K., and Nagayama M. (1976) The effect of ferric
hydroxide on the oxygenation of ferrous ions in neutral solution.
Corrosion Sci. **16**, 197–207.

Teng H. H. and Dove P. M. (1997) Surface site-specific interactions of
aspartate with calcite during dissolution: Implications for biominer-
alization. *Am. Min.* **82**, 878–887.

Van Cappellen P., Charlet L., Stumm W., and Wersin P. (1993) A
surface complexation model of the carbonate mineral-aqueous solu-
tion interface. *Geochim. Cosmochim. Acta* **57**, 3505–3518.

Wagner C., Gale H., and Raymond R. (1979) Two-dimensional chem-
ical state plots: A standardized data set for use in identifying chem-
ical states by x-ray photoelectron spectroscopy. *Anal. Chem.* **51**,
466–482.

Wehrli B. (1990) Redox reactions of metal ions at mineral surfaces. In
Aquatic Chemical Kinetics (ed. W. Stumm), pp. 311–336. Wiley.

Wersin P., Charlet L., Karthein R., and Stumm W. (1989) From
adsorption to precipitation: Sorption of Mn^{2+} on $FeCO_3$(s).
Geochim. Cosmochim. Acta. **53**, 2787–2796.

Westra K., Mitchell A., and Thompson D. (1993) Tip artifacts in
atomic force microscope imaging of thin films. *J. Appl. Phys.* **74**,
3608–3610.